Materials Advances

ROYAL SOCIETY OF CHEMISTRY

PAPER

View Article Online
View Journal | View Issue

Cite this: *Mater. Adv.*, 2026, 7, 469

The solvent stability of bromovirus allows for delivery of hydrophobic chemotherapeutic drugs

Elizabeth Loredo-García,[ab] M. Mariana Herrera-Hernandez,[ab] Carlos Medrano-Villagómez,[ab] Pierrick G. J. Fournier,[b] Ana G. Rodriguez-Hernandez,[a] Marcos Loredo-Tovías,[c] Jaime Ruiz-Garcia,[c] Bogdan Dragnea[de] and Ruben D. Cadena-Nava *[a]

Breast cancer is one of the main causes of mortality in women, and chemotherapy remains a fundamental pillar in its treatment. Although chemotherapy remains a mainstay in the treatment of breast cancer, the hydrophobicity and instability of drugs such as camptothecin (CPT) hinder their administration and bioavailability in aqueous media. To improve their solubility and stability, it is necessary to use suitable solvents that allow their encapsulation in nanovehicles without compromising their functionality. In this study, the use of viral nanoparticles (VNPs) derived from brome mosaic virus (BMV) and cowpea chlorotic mottle virus (CCMV) as platforms for the controlled delivery of CPT was investigated, evaluating the stability of the bromovirus in different polar solvents (methanol, ethanol, isopropanol, and DMSO). It was found that the viruses remain stable up to a concentration of 50% in all solvents for at least seven days, except in ethanol and isopropanol, where stability is maintained up to 30%. DMSO proved to be the optimal solvent, as it preserved their size and, in addition, favored trapping CPT in VNPs. Drug entrapment was more efficient in BMV, with a 30% higher uptake compared to CCMV when DMSO-PBS was used. *In silico* analysis using Autodock Vina revealed that drug retention occurs through hydrophobic interactions and hydrogen bonds between viral CP and camptothecin. The computationally predicted amount of drug entrapped in virions agrees with experimental results. *In vitro* studies in MDA-MB-231 cells confirmed the internalization of these bromovirus VNPs in the cell nucleus and a 50% higher cytotoxicity compared to free CPT. These findings highlight the potential of plant VNPs as an innovative platform for the enhanced delivery of hydrophobic drugs in the treatment of triple negative breast cancer and other diseases.

Received 21st March 2025,
Accepted 15th September 2025

DOI: 10.1039/d5ma00261c

rsc.li/materials-advances

Introduction

Cancer is one of the most frequent pathologies leading to fatalities and affects populations worldwide. It can be defined as a cellular disorder in which cells divide abnormally, ignoring normal cellular homeostasis, and resulting in the uncontrolled growth of cell aggregates (tumors) that damage neighboring tissues and alter their physiology.[1] Breast cancer is a major cause of mortality among women worldwide. Despite advances in the development of new therapies, chemotherapy remains a fundamental pillar in its treatment, especially in cases of aggressive breast cancer, such as triple-negative breast cancer (TNBC), which lacks hormone receptors and HER2, limiting targeted therapeutic options.[2,3]

Triple-negative breast cancer is more aggressive and does not respond effectively to hormonal modulators, so chemotherapy is recommended. Within the chemotherapeutic arsenal, camptothecin (CPT) is a broad-spectrum anti-tumor pentacyclic alkaloid derived from the *Camptotheca acuminata* tree, with demonstrated potential for significant cytotoxicity toward cancer cells. It acts by suppressing the enzyme topoisomerase I (TOP1), an enzyme involved in DNA replication, located ahead of the replication fork, where it is responsible for releasing tension to prevent DNA from supercoiling. The CPT inhibits DNA synthesis by strand scission, causing cell death during the S phase of the cell cycle.[4,5] The resistance generated towards CPT is due to both the mutations generated in transmembrane proteins that reduce the intranuclear accumulation of the drug.[6] In addition, the hydrolysis of CPT at physiological pH

[a] *Centro de Nanociencias y Nanotecnología – Universidad Nacional Autónoma de México (UNAM) – Ensenada, Baja California, México. E-mail: rcadena@ens.cnyn.unam.mx*
[b] *Centro de Investigación Científica y de Educación Superior de Ensenada, Baja California, (CICESE), Ensenada, Baja California, México*
[c] *Instituto de Física, Universidad Autónoma de San Luis Potosí (UASLP). San Luis Potosí, San Luis Potosí, México*
[d] *Department of Chemistry, Indiana University, Bloomington IN 47405, USA*
[e] *CIFRA, Magurele, Romania*

leads to the loss of activity. Therefore, drug carriers offering protection of CPT against these factors would increase the chemotherapeutic impact. The addition of targeting moieties could decrease the required dosage.

One of the strategies that helps overcome drug solubility, specificity, and stability challenges is using nanocarriers, which allow the drug molecule to be transported while preserving its functional attributes.[7] Nanocarriers can be synthesized from biological or synthetic materials. They can perform highly specific controlled drug delivery, improving their efficacy, increasing their target tissue accumulation, and reducing side effects such as systemic toxicity. In particular, they can reduce the toxicity of drugs such as the CPT0001 prodrug.[8] These advantages enable nanocarriers to overcome some of the limitations of conventional therapies and optimize the targeted delivery of therapeutic agents.

Virus-like particles (VLPs) in particular are nanocarriers that lack the genetic material of the virus but borrow the functional capabilities of its cage protein to protect and deliver encapsulated cargo. VLPs are non-infectious and can be used to efficiently transport bioactive molecules due to their high biocompatibility and water solubility. Virus nanoparticles (VNPs) maintain the genes of the virus; however, when plant viruses or bacteriophages are used, they are not infectious in humans, and they are ideal for functionalization and drug delivery.[9] Alternative nanocarriers, such as lipid nanolipospheres, are also effective for encapsulating hydrophobic drugs. Although they can exhibit instability over time, encapsulation in virus-like particles (VLPs) enhances their stability and ensures a more uniform size (Loredo-Tovias *et al.*, 2017).[7] However, the process of encapsulating nanolipospheres in VLPs can be somewhat labor-intensive, which may increase the cost of their synthesis. Therefore, an alternative is VNPs from plant viruses for transporting anticancer molecules.

Cowpea chlorotic mottle virus (CCMV) and the brome mosaic virus (BMV), which belong to the Bromovirus genus, are among the most investigated small icosahedral viruses. They contain ssRNA, and their protein shell called capsid is composed of 180 identical proteins arranged with T = 3 icosahedral symmetry. Both viruses have a diameter of $\sim$28 nm.[10] Recently, the effectiveness of plant VLPs has been shown with siRNA *in vitro* and *in vivo*, demonstrating the viability of these strategies in the targeted treatment of triple-negative breast cancer tumors.[11,12] However, loading plant viruses with hydrophobic anticancer molecules requires the use of solvents. Dimethyl sulfoxide (DMSO) is an aprotic solvent that is widely used to solubilize drugs, as well as different types of alcohol (protic solvents), such as ethanol, isopropanol, and methanol, but these solvents are also widely used as virucidal agents for a wide range of viruses.[13–15] Therefore, in this work, the stability of plant viruses in different solvents is studied, to provide a knowledge platform from which to synthesize CPT-loaded VNPs.

Along with stability experiments, to characterize the drug cargo/capsid interaction, molecular docking has been carried out. This *in silico* technique, widely applied in *in silico* drug development, predicts the strength of the interaction between a small molecule and a protein, facilitating an understanding of fundamental biochemical processes at the atomic level. Based on the 3D structure of proteins, AutoDock Vina uses the computational electrostatics of the complex to predict the expected experimental binding modes. Therefore, our research began with silico experiments, where the molecular docking between CPT BMV and CCMV proteins was examined, to evaluate possible drug conformations in viruses.[16]

Materials and methods

Production of BMV and CCMV

BMV and CCMV viruses were propagated on cowpea and barley plants. The seeds of each plant were sown in pots inside a greenhouse. Two weeks after germinated seeds were planted, the plant leaves were superficially damaged by mechanical abrasion with fine metal fiber. Subsequently, the plants were infected with 20 μL of a viral solution at 0.2 mg mL^{-1} in an inoculation buffer (0.01 M sodium phosphate and 0.01 M magnesium chloride, pH 6). The plants were harvested once they showed symptoms of infection (chlorosis), weighed, and stored at −20 °C until use.

Virus purification was performed by grinding the infected leaves with extraction buffer (0.5 M sodium acetate, 0.08 M magnesium acetate, 0.015% β-mercaptoethanol, pH 4.5) using a blender. The solution was then filtered using a cheesecloth to remove solid debris. Chloroform was then added at 4 °C and the samples were shaken for 10 minutes at 4 °C. The mixture was then centrifuged at 10 000 rpm for 20 minutes at 4 °C. Then the upper phase was recovered, and PEG 8000 was then added up to 10% w/v, and the sample was stirred overnight at 4 °C. It was centrifuged again and the pellet obtained was resuspended in SAMA buffer (sodium acetate 0.05M + magnesium acetate 0.008M). The sample then underwent ultracentrifugation on a 10% sucrose cushion at 32 000 rpm for 2.5 hours at 4 °C. The recovered pellet was resuspended in the SAMA buffer. The quantification of the concentration and purity of the viruses was assessed by using a UV-vis spectrophotometer Nanodrop (2000c, Thermo Scientific). Finally, the purified virus was stored at −80 °C.

The hydrodynamic diameter of the virus and VNPs was determined *via* dynamic light scattering (DLS) by using a Zetasizer NanoZS® (Malvern Instruments, UK). The samples were deposited on the carbon-coated copper grids (400 mesh) and stained with 2% uranyl acetate to be analyzed using a transmission electron microscope (TEM). The TEM Hitachi HF-3300 was operated at 100 keV and the images were taken at 40k× and 70k× magnifications.

Stability of BMV and CCMV in different solvents

The stability of the virus was evaluated in different solvents: isopropanol, ethanol, ethanol, and dimethyl sulfoxide at five concentrations: 50%, 30%, 20%, 10%, and 0% in SAMA buffer. For each condition, 100 μg of virus was used in 500 μL of buffer and incubated at 4 °C with slow shaking for 1 day and 7 days.

The samples were analyzed by DLS. Those samples that appeared free of aggregates by DLS at high solvent concentrations were then visualized by TEM.

Molecular docking of camptothecin to BMV and CCMV

In silico analysis of the capsid proteins of BMV and CCMV was performed to determine the sites available for docking with camptothecin. The 3D model of camptothecin ($C_{20}H_{16}N_2O_4$) was obtained from PubChem®. The 3D models of the viral proteins of BMV (3j7l) and CCMV (1za7) were obtained from the Protein Data Bank (PDB). In Autodock Tools®, the computational calculation was optimized by removing two of the three proteins in the trimer capsid protein. The proteins were divided into four sections using a "Grid Box." The molecular docking calculation was performed in Autodock Vina®. The binding sites were validated by repeating the program 100 times.

Docking sites were analyzed in PyMOL®, and the interactions at each site were examined in LigPlot+®. Finally, the mass of camptothecin ($g(m)_f$) was calculated according to the molecular docking sites found using eqn (1). Where g_v is the grams of virus (BMV or CCMV), and P_v is the weight of the virus protein, 4.6×10 g mol^{-1}. M_{pp} is the camptothecin molecules per protein calculated *in silico* multiplied by 180 capsid proteins of BMV or CCMV virus. PM_f is the molecular weight of camptothecin, 348.4 g mol^{-1}.

$$g(m)_f = \frac{g_v \times P_v \times M_{pp} \times 180}{PM_f} \quad (1)$$

Camptothecin was characterized using fluorimetry to obtain its excitation and emission spectra at different concentrations of dimethyl sulfoxide (DMSO) in phosphate-buffered saline (PBS). The results were obtained using a fluorescence spectrophotometer (Agilent Cary Eclipse G9800A).

Camptothecin loading in viruses

A stock of 1 mg mL^{-1} of camptothecin was prepared in DMSO. To synthesize VNPs, 200 μg of virus was incubated in 80 μL of PBS with 50% of DMSO containing different concentrations of CPT. Samples were gently shaken in the LabRoller for 1 hour at 4 °C in the dark. The obtained VNPs were purified and concentrated by ultrafiltration with 100 kDa Amikon filters, at 3000 G for 30 min, to remove DMSO and the drug not coupled to the virus. Finally, the VNPs in PBS buffer were stored at 4 °C protected from light.

The amount of drug coupled to the virus was calculated from fluorescence curves at different concentrations of camptothecin. The size of the VNPs was evaluated by DLS, while their morphology was evaluated by TEM. The drug release assay was carried out at different pH values using high-performance liquid chromatography (HPLC, Agilent). A calibration curve was obtained at different concentrations of camptothecin, using a fluorescence detector and a reverse-phase column (eclipse XDB). The elution gradient was Milli-Q water (pH 7) to 60% acetonitrile in 20 minutes with a flow rate of 0.3 mL min^{-1}, with camptothecin monitoring at 367 nm. Camptothecin-loaded VNPs were placed on a 14 kDa dialysis membrane at 100 ng μL^{-1} (drug), at 4 °C in the dark for 1 and 24 hours, under pH conditions of 4, 5, 6, and 7. Then, the released camptothecin from the VNPs was analyzed by HPLC using the same elution procedure as described for the calibration curve.

Cell culture

The triple-negative epithelial human breast cancer cell line MDA-MB-231/GFP (AKR-201 Cell Biolabs) was used to measure the efficacy of camptothecin-loaded VNPs. This cell line constitutively expresses green fluorescent protein (GFP). MDA-MB-231 (ATCC) were used in the mitochondrial assay. The cells were cultured using DMEM (Thermo Fisher Scientific) supplemented with 10% fetal bovine (Biowest) serum and 1% antibiotic/antimycotic (Thermo Fisher Scientific). Cells were incubated at 37 °C with 5% CO_2 and subcultured when they reached 80% confluence. For subculture, cells were trypsinized with trypsin-EDTA (Thermo Fisher Scientific), centrifuged, and counted using a Neubauer chamber with trypan blue as a cell viability control. 250 000 cells per dish were seeded.

Cell internalization

Preparation of NanoOrange-labeled VNPs. The NanoOrange (NOr) working solution was prepared according to the supplier's specifications and to the virus labeling protocol described by Nuñez-Rivera *et al.*[11] 2.15 μL of NOr working solution was used per μg of VNPs, maintaining a 5 : 1 volume ratio of NOr to VNPs. The mixture was shaken for 30 minutes at 4 °C in the dark. The labeled VNPs were then purified by ultrafiltration using Ultracel® filters (30 kDa MWCO), 3500 rpm for 20 minutes at 4 °C, repeating the process five times with PBS buffer. Finally, the labeled VNPs were stored at 4 °C protected from light. To verify the labeling, the fluorescence of the samples was observed by radiation with excitation at 488 nm and emission at 570 nm in the Cary Eclipse Fluorescence Spectrometer (Agilent).

Internalization of VNPs in MDA-MB-231 cells. Glass coverslips were functionalized with Poly-L-Lysine (Sigma Aldrich) to allow cell adhesion by placing 200 μL on each coverslip for 20 minutes under sterile conditions, followed by three washes with PBS. After 24 hours, 100 000 cells were seeded on each coverslip and incubated to allow adhesion. The complete medium was then added and incubated for 24 hours at 37 °C and 5% CO_2. To synchronize cells in the G0/G1 phase, the complete medium was removed, and they were incubated with unsupplemented DMEM for 12 hours. Subsequently, cells were then treated with NanoOrange (NOr)-labeled VNPs containing 24 ng μL^{-1} of camptothecin for 4 hours. After treatment, cells were fixed with 4% glutaraldehyde, permeabilized, and blocked to avoid image artifacts. Cell nuclei were labeled with DAPI and washed to remove excess. Finally, coverslips were mounted onto slides and samples were observed by confocal microscope (Olympus FV1000). Micrographs for cell reconstruction were recorded and analyzed by FV10-ASW 4.2 Viewer and confocal micrographs were acquired from optical sections with 0.4 μm thickness. Images of DAPI (405 461 nm)-labeled nuclei (blue), GFP (488/509 nm)-fluorescent cytoplasm (green), and NanoOrange (543/570 nm)-labeled VNPs (orange) were obtained at 60× magnification.

Cell viability

The cytotoxicity of the VNPs was assessed by measuring the cellular metabolic function using an MTT-based *in vitro* toxicology assay KIT (Sigma Aldrich). 20 000 cells per well were seeded in 96-well plates and 80 μL of complete medium (DMEM) was added. Different concentrations of VNPs were then added in 20 μL of PBS buffer. The cells were incubated for 24 hours at 37 °C with 5% CO_2. Afterward, 10 μL of MTT solution was added and the cells were incubated for another 4 hours. The formazan crystals formed were solubilized with 100 μL of lysis solution (acidified isopropanol, MTT Kit) and the absorbance was measured at a wavelength of 570 nm.

Mitochondrial permeability assay

Changes in the mitochondrial membrane potential (MMP) of the MDA-MB-231 cells exposed to VNP treatments were assessed using the cationic dye JC-1 (MitoID Red), which fluoresces green with a resting membrane potential (−150 mV to −180 mV) and orange with an active membrane potential (−140 mV to −200 mV). The cell nuclei were incubated with Hoechst 33342 and the mitochondria were stained with MitoID Red (1 : 1500) in PBS/Tween 0.3% (v/v) for 1 hour at 37 °C, then washed. Confocal images were taken with excitation wavelengths of 558 nm (for high MMP) and 488 nm (for low MMP). Densitometric analysis of fluorescence intensity was performed using ImageJ® by calculating the percentage of mitochondrial area in the cytosol and the orange/green fluorescence ratio for each image.

Results and discussion

Stability assay of BMV and CCMV

The stability of BMV and CCMV viruses (Fig. S1) in different organic solvents was evaluated, because CPT is hydrophobic, and it is necessary to use solvents for loading into the virions without altering their stability. Methanol, ethanol, isopropanol, and DMSO were tested in different proportions (V : V) mixed with SAMA buffer. Results showed that the pH of the mixtures increased as the solvent proportion increased (Fig. S2), ranging from 4.5 to 6.0, with no significant differences between the solvents. This is significant because, at a higher, near-neutral pH, bromoviruses undergo a swelling transition that increases capsid permeability. This well-characterized phenomenon illustrates the responsive nature of the viral capsid to environmental chemical cues. Native viruses were evaluated to compare their morphology and size with those observed after exposure to solvents. For BMV, the average size was 30.04 ± 1.39 nm (Fig. S1A and B), which coincides with the average hydrodynamic diameter obtained by DLS, 28.21 nm (Fig. S1C). For CCMV, the average size was 30.70 ± 1.44 nm (Fig. S1D and E), and the average hydrodynamic diameter was also 28.21 nm (Fig. S1F).

The hydrodynamic diameter of the BMV and CCMV virions did not change when exposed to different concentrations of DMSO. However, in methanol, the viruses showed a decrease in average diameter to 24.4 nm with 10% of the solvent, an effect that was maintained up to 50%. Ethanol and isopropanol caused a progressive size reduction with increasing concentration, and the size of the viral particles could not even be measured at 50% of these solvents (Fig. 1A and B). ANOVA analysis (Tukey test) revealed that both ethanol and isopropanol significantly affected the BMV virions while increasing the solvent concentration up to 50%. For CCMV, isopropanol destroyed the virions, while ethanol at concentrations of 20% and 30% reduced the diameter of the virions. According to Hasan *et al.*, methanol is rarely used in health care because it has a lower level of disinfection compared to ethanol and isopropanol.[17] In contrast, ethanol is an effective virucidal agent, inactivating 60–80% of all lipophilic viruses and various hydrophilic viruses. On the other hand, isopropyl alcohol has some activity against non-lipid viruses but is highly effective against lipid viruses, such as COVID-19. The most likely mode of action of alcohol against non-lipid viruses is protein denaturation.[18]

Fig. 2 shows the TEM micrographs of BMV exposed to different solvents. When BMV was in 30% ethanol, the micrograph showed dispersed virions, however, there were also protein clumps, and the

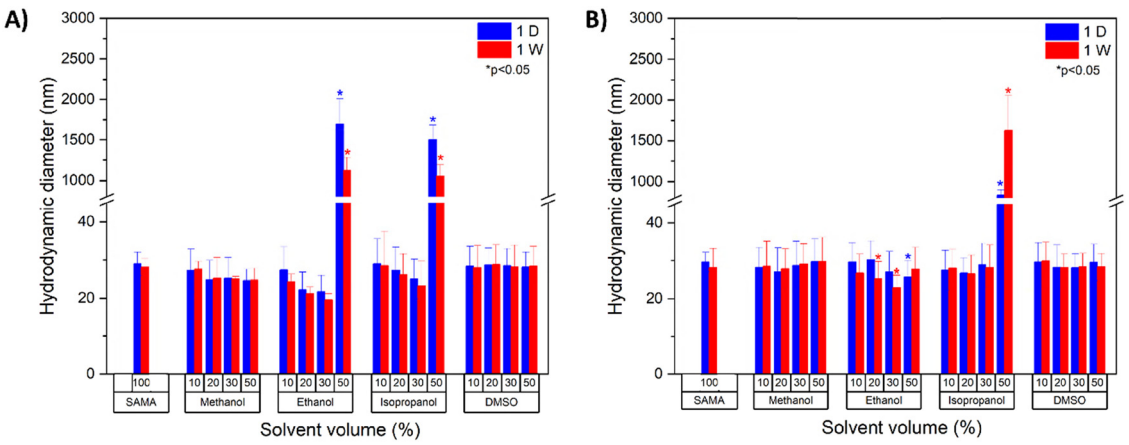

Fig. 1 Hydrodynamic diameters. Obtained by DLS, diameters of BMV and CCMV after being incubated in the solvent mixtures for 1 day (blue) and 7 days (red). (A) Hydrodynamic diameters of BMV with solvent mixtures and SAMA buffer. (B) Hydrodynamic diameters of CCMV with solvent mixtures and SAMA buffer. Bars represent the average diameter, and error bars represent the standard deviation (SD). Means and standard deviations are reported in Table S1. Statistical analyses One-way ANOVA, Tukey test, $*P < 0.05$.

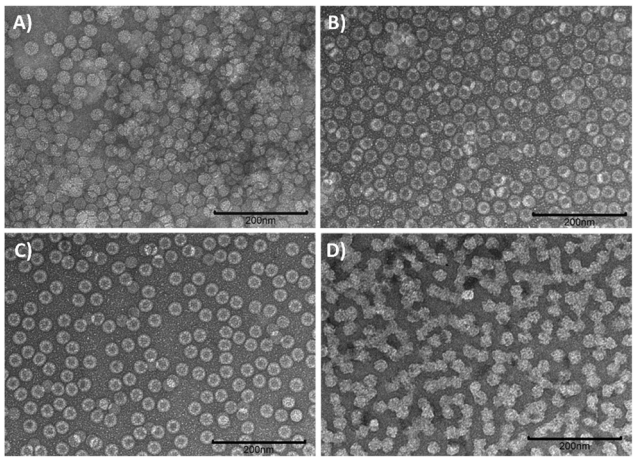

Fig. 2 TEM micrographs of BMV in different solvents. (A) Micrograph of BMV viruses in 30% ethanol. (B) Micrograph of BMV viruses in 30% isopropanol. (C) Micrograph of BMV viruses in 50% methanol. (D) Micrograph of BMV viruses in 50% DMSO. Magnifications 40 k×, scale 200 nm.

measured diameters of BMV were 22.6 ± 1.7 nm (Fig. 2A). Whereas, when BMV is in 30% isopropanol, the virions were found in a dispersed manner with few clumps, and the average diameter was 23.2 ± 2.5 nm (Fig. 2B). For BMV in 30% methanol, the virions were found in a dispersed manner with some clumps, and the average diameter was 26.2 ± 2.7 (Fig. 2C). Finally, the BMV virions in 50% DMSO were most dispersed (Fig. 2D), with small agglomerates, and the size distribution of the viruses was 25.9 ± 3.6 nm (size histograms in Fig. S3). The ANOVA of the sizes obtained by TEM coincides with the data from DLS, with no significant differences between the control group of BMV in SAMA buffer and BMV in DMSO at 50% or in 50% methanol, however, ethanol and isopropanol significantly affect the size of BMV.

Fig. 3A shows the CCMV in a 50% ethanol mixture, the micrograph shows dispersed virions, and the measurement of the CCMV diameter was 24.2 ± 2.5 nm. Fig. 3B shows BMV in 30% isopropanol, virions were found in a dispersed manner with areas of virus and protein agglomeration, and the average diameter was 22.5 ± 2.2. Fig. 3C shows CCMV in 30% methanol, the virions were found in a dispersed manner, and the average diameter was 26.6 ± 2.9. Fig. 3D shows the CCMV virions in DMSO at 50%, the virions are dispersed, with some areas with agglomerations and some virions begin to deform, the diameters were 27.9 ± 2.7 nm (size histograms in Fig. S4). The sizes obtained by TEM coincided with the trend marked in the DLS data, however, the ANOVA of the data obtained by TEM shows that there are no significant differences between the control group of CCMV in SAMA buffer with 50% methanol, 30% isopropanol, 50% ethanol, and 50% DMSO.

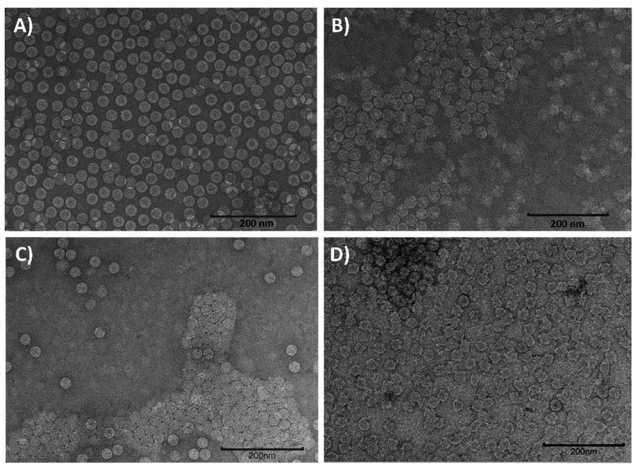

Fig. 3 TEM micrographs of CCMV in different solvents. (A) Micrograph of CCMV viruses in 50% ethanol. (B) Micrograph of CCMV viruses in 30% isopropanol. (C) Micrograph of CCMV viruses in 50% methanol. (D) Micrograph of CCMV viruses in 50% DMSO, magnifications 40 k×, scale 200 nm.

Overall, DMSO did not significantly affect the stability and morphology of the virions after 7 days of incubation, the results are consistent with those of Xie *et al.*, who mentioned that the hydrophobic interactions that stabilize BMV capsids partially function in mixtures of DMSO and water, since DMSO preferentially binds to the random sites of the viral protein and the β-pleated sheet region is mainly responsible for intercapsomeric interactions.[19] In addition, Bond *et al.*, found that BMV capsids disassemble abruptly when the pH was increased around 10.5 or when the ionic strength increased at neutral pH. In contrast, the alcohols evaluated caused disassembly of the capsids at high concentrations due to the loss of intermolecular forces, such as hydrogen bonding and hydrophobic forces.[20] According to Wanguyun *et al.*, the hydrophobic forces that keep viruses assembled are strengthened when in contact with water.[21] However, when alcohol is added, these forces are weakened and the proteins acquire a certain degree of movement, which destabilizes the capsid and causes it to disassemble. The results suggest that DMSO is the most suitable solvent for loading virions since it does not significantly alter their stability, while alcohols can destabilize them at high concentrations.

In silico analysis quantification of camptothecin docked to BMV and CCMV

The monomer structure was extracted directly from the experimentally resolved structure of the assembled trimeric capsomere, meaning it retains its physiological conformation from the viral capsid. Furthermore, since our experimental loading was performed on pre-assembled capsids, the protein–protein interfaces were already occupied and structurally locked, making them experimentally inaccessible to CPT molecules. Therefore, our model, which focuses on internal surfaces and pockets away from these interfaces, remains highly relevant. While performing docking on a complete capsid is computationally complicated, our simplified approach consistently identified internal hydrophobic binding regions, a finding strongly supported by CPT's well-documented behavior in other systems.[22,23]

Tables S1 and S2 show the *in silico* molecular docking analysis performed with Autodock Vina®, which identify 11 CPT molecules capable of binding to BMV with affinity energies between −7.3 and −5.2 kcal mol^{-1}. In the case of

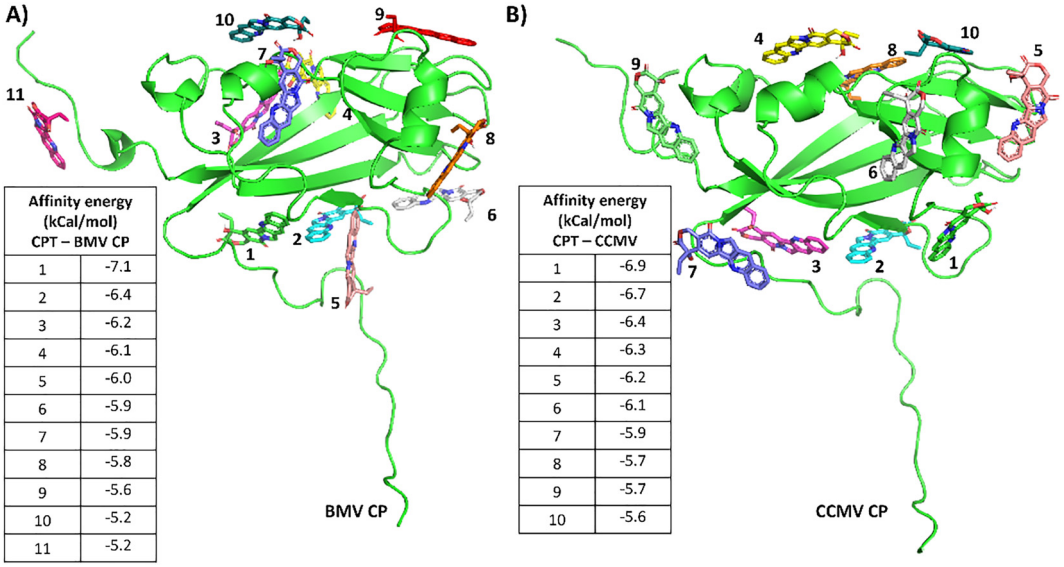

Affinity energy (kCal/mol) CPT – BMV CP	
1	-7.1
2	-6.4
3	-6.2
4	-6.1
5	-6.0
6	-5.9
7	-5.9
8	-5.8
9	-5.6
10	-5.2
11	-5.2

Affinity energy (kCal/mol) CPT – CCMV	
1	-6.9
2	-6.7
3	-6.4
4	-6.3
5	-6.2
6	-6.1
7	-5.9
8	-5.7
9	-5.7
10	-5.6

Fig. 4 Molecular docking between the drug CPT and BMV and CCMV proteins. (A) Docking between CPT and BMV protein, and (B) docking of CPT and CCMV protein.

cowpea chlorotic mosaic virus (CCMV), 10 CPT molecules were found with affinity energies between −6.9 and −5.6 kcal mol^{-1}. Fig. 4A shows the CPT molecules that can dock to the BMV protein, CPT docks around the protein, including in the C-terminal region, the protein–protein interaction region. When using viruses at acidic pH, the CPT could not bind in these regions because there are sites occupied by interactions between proteins. However, at neutral and basic pH, the capsid swells, and the protein–protein interactions can change. Fig. 4B shows the CPT molecules that can be coupled to the CCMV protein. Similar to BMV, the CPT is distributed throughout the viral protein and the number of molecules that can be coupled is lower compared to the amount that can be coupled to the BMV protein. The finding that the highest-affinity drug binding sites are located on the inner surface of the capsid in both viruses indicates that viral capsids are well-suited for use as nanovehicles, as their structure naturally facilitates cargo encapsulation.

Fig. S5 shows two examples of the types of interactions found between CPT and BMV, and CPT and CCMV; in both cases, hydrophobic interactions are observed (red bars) while the green dotted lines indicate hydrogen bonds. In the case of CCMV, 10 CPT molecules were docked with affinity energies between −6.9 and −5.6 kcal mol^{-1}. The interactions between CPT and the viral protein occur mainly through hydrophobic interactions, with 85.5% for BMV and 90.4% for CCMV. Hydrogen bonds are also observed (14.5% for BMV and 9.6% for CCMV) thanks to the nitrogen and oxygen present in the lactone ring of CPT. The amounts of drug that virions can load were calculated, using eqn (1), 29.9 μg for BMV and 27.2 μg for CCMV, *i.e.*, 11 CPT molecules for BMV CPT and 10 CPT for CCMV CPT. Therefore, the identified CPT docking sites could differ if the simulation was performed on the entire virion rather than an isolated monomer. Nevertheless, CPT's hydrophobic nature suggests a strong preference for burial within the protein's internal regions. This is consistent with prior studies showing CPT embeds within hydrophobic pockets of lipid or protein complexes,[22,23] and it supports our *in silico* finding that CPT predominantly lodges at the internal interface of the bromovirus capsid protein.

Synthesis of VNPs: camptothecin loading into viruses

The synthesis of VNPs consisted of three simple steps described in Fig. 5. In the first, the purified viruses were mixed with different concentrations of CPT in different buffers with 50% DMSO, then, the VNPs were left under gentle agitation for 1 h at 4 °C and finally VNPs were purified by ultrafiltration with the 100 kDa filter. Increasing concentrations of camptothecin (CPT) were used to determine the optimal drug loading into BMV virions, with concentrations of 30 μg, 65 μg, and 100 μg corresponding to 1908, 4100, and 7000 molecules per virion. In addition, three loading buffers were evaluated to identify the one that best favors molecular docking. Fig. 6A shows the DLS graph of the different BMV-CPT compositions in SAMA buffer, which shows that all compositions have a diameter of around 28.2 nm, data that are corroborated by the micrograph of the BMV-CPT 7000 composition in SAMA buffer (Fig. 6B), where sizes of 26.83 ± 2.38 are observed (Fig. S6A). In Fig. 6C, BMV-CPT in TNKM buffer exhibits a main hydrodynamic diameter of around 32.7 nm, however, there is also a prominent peak around 1000 nm. The micrograph of the BMV-CPT 7000 composition (Fig. 6D) shows large VNPs, incomplete virions, and proteins, the size distribution ranged from 20 to 70 nm (Fig. S6B), with an average size of 42.47 ± 13.64. In Fig. 6E, the DLS graph of the different BMV-CPT compositions in PBS buffer shows the hydrodynamic diameter of 32.7 nm. While in the micrograph of the BMV-CPT 7000 composition in PBS buffer (Fig. 6F), large VNPs are observed, with an average size

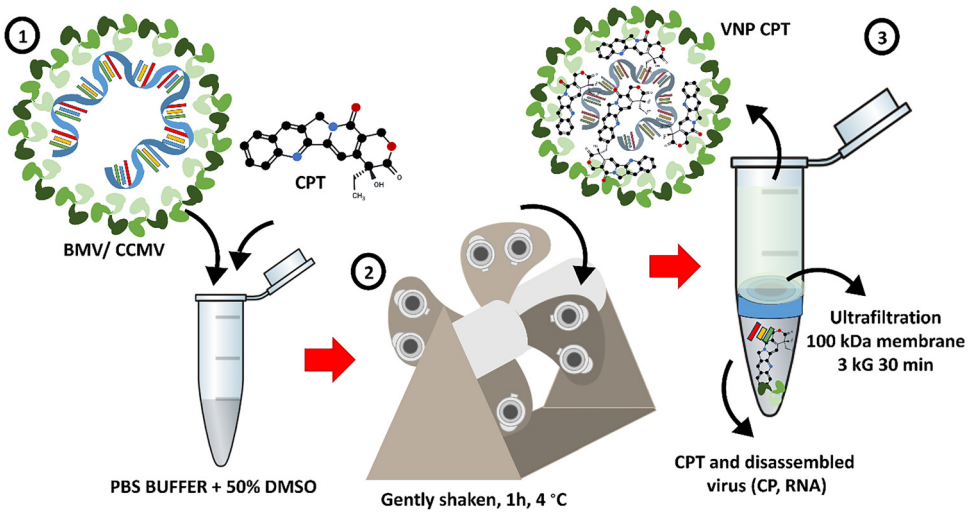

Fig. 5 Camptothecin loading into virus particles. Virions were incubated in PBS containing 50% DMSO and varying concentrations of CPT. The samples were gently shaken for 1 hour at 4 °C in the dark. The resulting drug-loaded virus-like particles (VNPs) were then purified and concentrated *via* ultrafiltration using 100 kDa Amicon filters at 3000×*g* for 30 minutes.

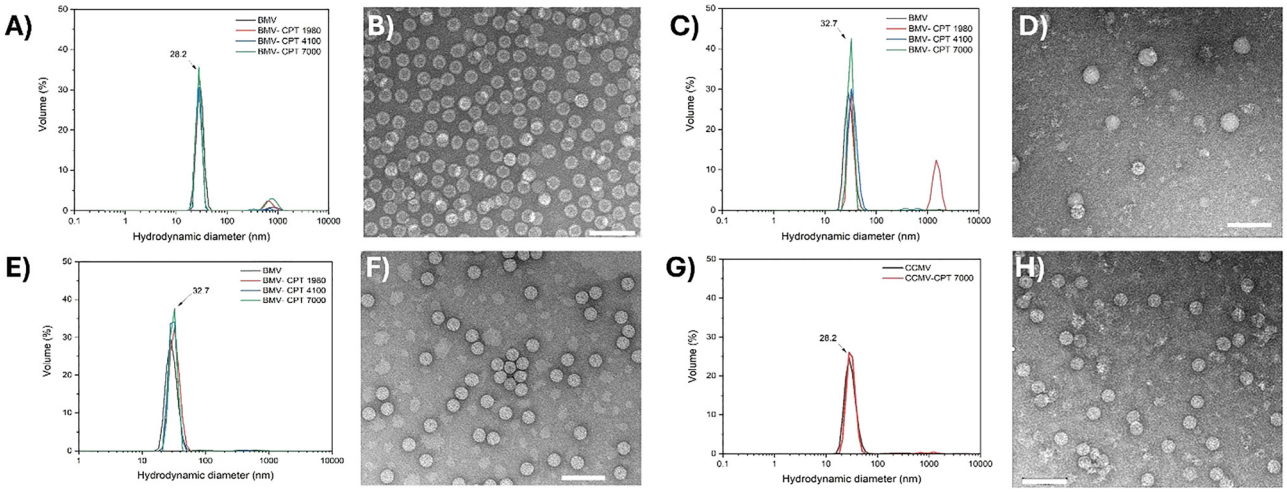

Fig. 6 Size of BMV-CPT VNPs in different loading buffers. (A) DLS size distribution of the different BMV-CPT compositions in SAMA buffer. (B) Micrograph of the BMV-CPT 7000 composition in SAMA buffer. (C) DLS size distribution of the different BMV-CPT compositions in TNKM buffer. (D) Micrograph of the BMV-CPT 7000 composition in TNKM buffer. (E) DLS size distribution of the different BMV-CPT compositions in PBS buffer. (F) Micrograph of the BMV-CPT 7000 composition in PBS buffer. (G) DLS size distribution of CCMV-CPT VNPs. (H) Micrograph of the composition of CCMV-CPT in PBS buffer. The scale bar corresponds to 100 nm. Means and standard deviations are reported in Table S4.

of 36.64 ± 4.9 (Fig. S6C). Fig. 5G shows that CCMV-CPT (Red) has a diameter of 30.97 ± 2.78 nm in PBS buffer, and Fig. 6H shows the micrograph corresponding to the CCMV-CPT VNPs, in which bigger virions with an average size of 36.5 ± 2.65 nm are observed (Fig. S6D).

To determine the concentration of camptothecin, a fluorimetry calibration curve was obtained using different concentrations (Fig. S7). Table 1 shows the results obtained by fluorimetry, where it is shown that a smaller amount of CPT is coupled to BMV when the process is carried out with SAMA buffer (pH 4.6), and TEM images and DLS analysis indicate that BMV viruses remain stable at an approximate CPT loading of ≈581 molecules per virion. However, when TNKM buffer (pH 7.4) is used a greater amount of CPT associates with the virion, approximately 687 molecules per virion. TEM images and DLS show an increase in size of approximately 30% compared to BMV without CPT. In addition, the DLS shows large particles that could be agglomerations due to virion disassembly, and TEM analysis also shows incomplete virions and protein aggregation. In contrast, in PBS buffer, the amount of CPT per BMV particle is approximately 2060 molecules per virion. TEM images show a diameter of ∼35 nm, monodisperse VNPs, an increase in size over 15% compared to BMV without the drug, Fig. 6F. These results agree with those reported by

Table 1 Drugs docked to BMV and CCMV capsids. The number of CPT molecules available and those docked to BMV and CCMV virions experimentally in different buffers. Mean ± SD, n = 3

Number of CPT molecules available per virion	Number of molecules docked per virion in different buffers		
	SAMA (pH 4.6)	TNKM (pH 7.4)	PBS (pH 7.4)
1980	0	264 ± 10	412 ± 38
4100	359 ± 18	634 ± 66	1004 ± 58
7000	581 ± 22	687 ± 84	2060 ± 81

Bond *et al.*, who mention that an expansion of around 10% of the virus capsid can be caused by the deprotonation of glutamic acid residues at pH higher than 6.2.[20] This expanded structure of the viruses allows the capsid pores to have diameters of ~2 nm. The pH-controlled change, increasing around pH 6 and 7.5, induces radial swelling of the virus and was hypothesized to be related to the assembly–disassembly mechanism of the protein capsid by decreasing the intercapsomeric hydrophobic attraction.[24] Meanwhile, ionic strength is responsible for the gradual loosening of the virus conformation by interfering with the stabilizing salt bonds, thereby decreasing the strength of protein–RNA interactions and leading to partial rupture of the virus.[25] That is why PBS buffer was established as a drug-loading buffer, and the number of molecules available for the coupling process was set at 7000 per virion. The experimentally estimated amount of CPT associated with BMV and CCMV indicates that BMV can carry a larger amount of drug, 4% more than that predicted by *in silico* assays. The experimental value for the amount of CPT associated with CCMV is about 19% less CPT associated with CCMV than the amount computationally predicted (Table 2).

The fluorimetry results corroborate the findings shown in the TEM micrographs. The BMV particle diameter increases significantly when loaded with CPT drugs, whereas the CCMV size remains unchanged. Experimental results show that the BMV can load 29.5% more CPT than the CCMV. The *in silico* results, however, indicate lower percentages (Table 2), with the BMV loading 9.1% more CPT than the CCMV. Additionally, the BMV loads 4% more CPT than the *in silico* prediction. Additionally, the BMV loads 4% more CPT than the *in silico* prediction. The difference in drug loading efficiency between CCMV and BMV may be attributed to differences in the number of hydrophobic binding sites on their respective capsid proteins. As shown in Fig. 4, molecular docking identified 11 potential CPT-binding sites on the BMV protein, compared to 10 on the CCMV protein. While this difference of a single site may seem minor per protein, it scales to a deficit of 180 hydrophobic sites per capsid for CCMV, given the T = 3 icosahedral architecture composed of 180 subunits. This substantial reduction could significantly impact the overall drug loading capacity.

Table 2 Comparison of the amount of drug coupled to BMV and CCMV capsids. Several CPT molecules are available and those are coupled to BMV and CCMV virions experimentally *vs in silico*. Mean ± SD, n = 3

Nanovehicle	Number of docked molecules per virion		
	PBS	*In silico*	PBS/*in silico* (%)
BMV-CPT	2060 ± 81	1980	104.0
CCMV-CPT	1453 ± 55	1800	80.72

These results could indicate that in addition to the coupling zones between the viral capsid and the drugs, the molecules could be internalized within the virion through the pores when the virus is in a neutral-basic environment. However, further *in silico* studies are required to predict the molecular dynamics and possible interactions of the drugs with the RNA of the virions.

Finally, a CPT release assay was performed at different pH values to simulate the behavior of the nanovehicles in different environments. CPT was characterized by HPLC. Fig. S8 shows the chromatogram at different concentrations of CPT. A decrease in fluorescence intensity can be observed as the concentration of the drug in solution decreases. Fig. 7 shows that BMV releases the highest percentage of CPT compared with CCMV at all the pH values. Also, for the CCMV-CPT, no release of CPT was detected after 1 hour.

In the drug release assay at different pH values, a clear trend is observed, the release of CPT increases as pH rises. In addition, the results show that BMV releases more CPT compared to CCMV at all tested pH values. This phenomenon could be related to the type of interactions formed between the drug and the proteins, as shown in the *in silico* study. Even though the proteins of both viruses share 80% sequence identity, the interaction sites and the amino acids involved are different. At pH 7, BMV released 44.59% of CPT, while CCMV released only 11.86%. Furthermore, TEM micrographs show that BMV-CPT are of larger sizes than CCMV-CPT. The mechanistic basis for

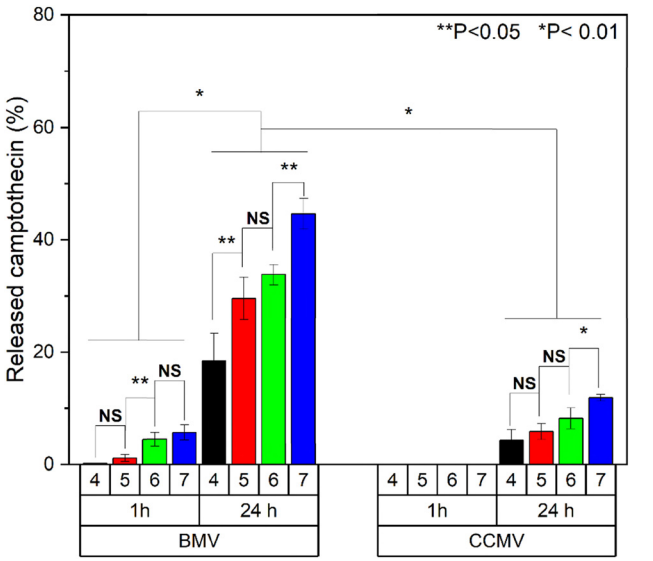

Fig. 7 Percentage of CPT released by dialysis. The amount of drug released increases with time and pH value. The numerical scale on the x-axis represents the pH. Bars represent the average of liberation, and error bars represent the standard deviation (SD). Statistical analyses included One-way ANOVA and Tukey test, $^{**}P < 0.05$, $^{*}p < 0.01$, NS means not significant. Means and standard deviations are reported in Table S5.

the differential drug release profiles between BMV and CCMV could be primarily attributable to their distinct swelling behaviors at neutral pH. Despite significant sequence homology, a critical difference exists: the BMV sequence is shorter by one residue due to deletions at positions 27 and 150, which are located at key protein–protein interaction interfaces. Notably, the deletion at position 27 perturbs the β-hexamer pore (residues 27–35). These structural variations give rise to significant conformational differences at the subunit level (RMSD 0.88–1.06 Å), thereby altering their dynamic properties. As a result, BMV exhibits a broader and more pronounced pH-dependent swelling transition, initiating between pH 6.0 and 7.0, compared to CCMV, which requires a pH of $\geq$7.0 in order to become swollen.[26] This heightened dynamic propensity of the BMV capsid to swell across a wider pH range correlates directly with our experimental observations, wherein BMV releases its loaded cargo more freely at all pH conditions tested, including the physiologically relevant pH of 7.4. The higher drug load in BMV may interfere with intercapsomeric interactions of the BMV viral proteins, making the VLP more susceptible to pH changes.

Cell culture

Cell internalization

NanoOrange labeled VNPs. *In vitro* assays were performed with the synthesized VNPs (nanovehicles) labeled with the NanoOrange fluorophore to study their internalization in human breast cancer cell line MDA-MB-231 using confocal microscopy. Fig. S9A shows the characterization of the targeted nanovehicles with the following hydrodynamic diameters: CCMV (red) of 24.4 ± 3.7 nm, BMV (gray) of 32 ± 4.5 nm, BMV-CPT (blue) of 37.8 ± 9.4 nm, and CCMV-CPT (green) of 28.2 ± 2.5 nm. The size of the NanoOrange labeled viruses VNPs increases concerning native viruses, however, no significant differences were found between the groups. Signals were observed in sizes larger than 100 nm, possibly agglomerated. Fig. S9B presents the emission spectrum of the labeled VNPs, with an emission maximum near 570 nm. In addition, NanoOrange labeled VNPs showed fluorescence emission at 560 nm, as previously reported by Nuñez-Rivera *et al.*[11]

Internalization of VNPs in MDA-MB-231 cells. Fig. 8 shows the internalization of viruses labeled with the NanoOrange fluorophore in MDA-MB-231 human breast cancer cells. The blue channel corresponds to DAPI, the green channel corresponds to GFP, and the orange channel is the NanoOrange molecule coupled to the VNPs. The treatments of BMV and CCMV labeled with NanoOrange, showed orange fluorescence in the cytoplasm and near the nuclei, indicating that the viruses were internalized. The negative control did not show NanoOrange fluorescence in the cytoplasm cultured cells. However, for BMV and CCMV labeled with NanoOrange and CPT, both orange and blue fluorescence were detected in the cytoplasm and nuclei, even without DAPI staining, the blue fluorescence corresponds to the CPT (Fig. 9), indicating the internalization of the VNPs. This suggests the internalization of BMV-CPT and CCMV-CPT with the co-localization of NanoOrange fluorescence and the CPT molecule in the nuclei, implying that both compounds remain bound to the viral proteins. These results

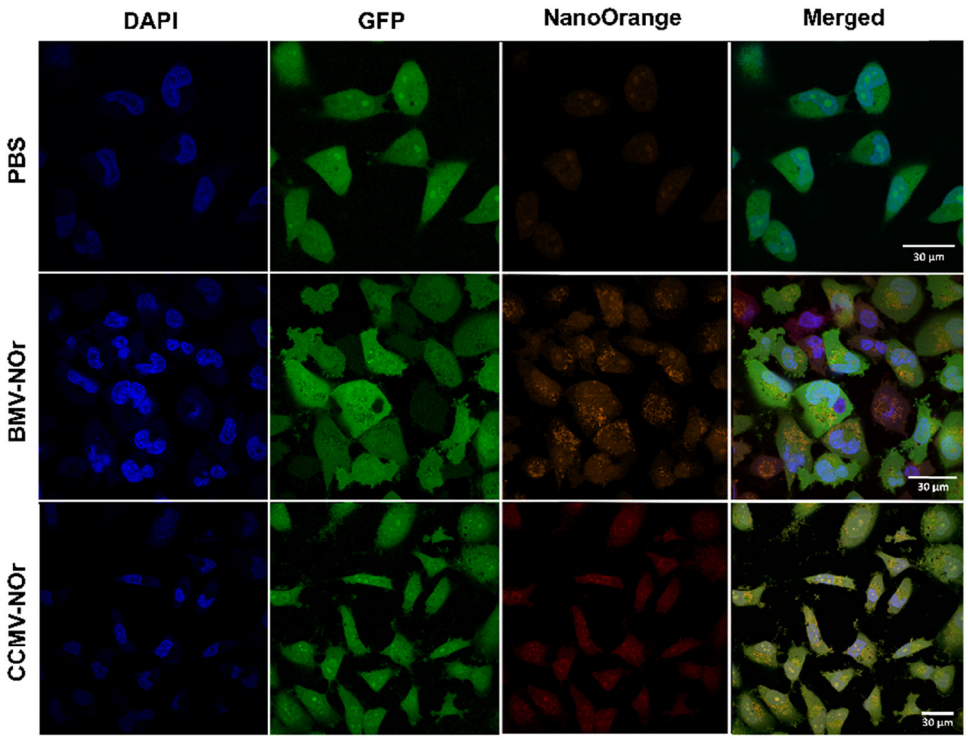

Fig. 8 Confocal micrograph of MDA-MB-231 cells. The blue channel corresponds to DAPI (nuclei). The green channel corresponds to GFP (cytoplasm). The orange channel corresponds to PBS, BMV-Nor or CCMV-NOr. Colocalization of the three channels.

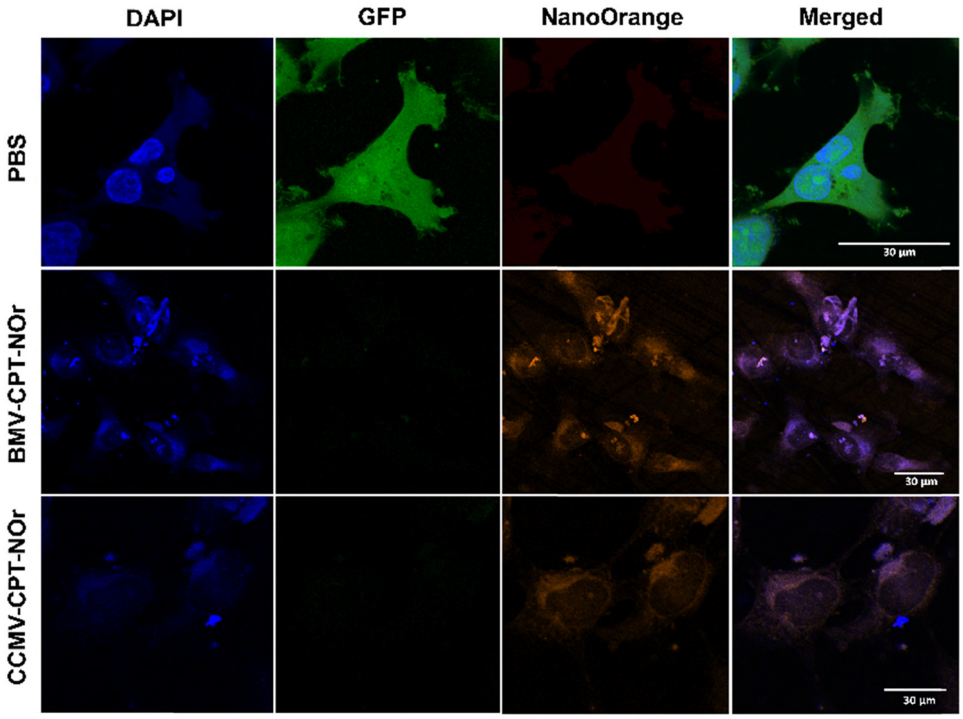

Fig. 9 Confocal micrograph of MDA-MB-231 cells with BMV-CPT-NOr and CCMV-CPT-NOr. The blue channel corresponds to DAPI (nuclei) or CPT. The green channel corresponds to GFP. The orange channel corresponds to NOr.

remarkably confirmed that VNPs are efficiently internalized into the nucleus of the MDA-MB-231 cells, where CPT acts, indicating their potential to transport drugs to the nucleus of the cancer cells. In this case, the cells were not stained with DAPI to be able to observe the fluorescence of the CPT, and the cytoplasm (green channel) is not observed because the cells were damaged, probably by the treatment.

The internalization of viruses and VNPs without functionalization was observed in MDA-MB-231 cells. Confocal microscopy results showed that the synthesized VNPs can be internalized into the cytosol of MDA-MB-231 cells, in addition, it was found that VNPs can enter the cell nucleus, the site of action of CPT.[6] The mechanism for cellular internalization of CCMV and BMV in animal cells is not yet fully defined. The large size of these VNPs precludes passive diffusion. Therefore, we hypothesize that this process is actively driven by intrinsic properties of the capsid. This hypothesis is strongly supported by the consistent internalization of BMV-based VLPs across diverse cell lines and with different cargos.[11,27,28] This intrinsic translocation capability may be rooted in the capsid's peptide sequences. Futaki *et al.* (2001) demonstrated that synthetic peptides derived from the N-terminus of the BMV capsid protein (CP) exhibit potent membrane translocation activity in macrophages, comparable to the well-known HIV-1 Tat-(48–60) peptide. A peptide derived from CCMV also demonstrated a moderate, though lesser, degree of translocation. Building on this precedent, we propose a possible mechanism for BMV and CCMV virions: following cellular uptake, the VNPs can undergo partial disassembly or swelling, thereby exposing N-terminal CP regions. These exposed peptides could then facilitate active transport of the particle or the released drug payload into the nucleus. However, this proposed mechanism remains speculative. Definitive validation of the precise cellular pathways involved—and the role of these intrinsic peptide sequences in the context of the complete capsid—constitutes essential and compelling work for future studies.

A significant challenge in nanocarrier design is the frequent requirement for surface functionalization to achieve efficient cellular uptake. For instance, Ghosh *et al.*, demonstrated that doxorubicin-loaded VLPs derived from Flock House virus (FHV) required conjugation to a tumor-homing peptide for internalization into MDA-MB-231 cells, while unconjugated VLPs were not internalized.[29] In striking contrast, the camptothecin (CPT)-loaded BMV and CCMV VLPs developed in the present study were efficiently internalized into malignant cells within four hours without any surface modification. This intrinsic targeting capability represents a notable advantage, simplifying the formulation process and potentially improving the translational pathway.

Cell viability

MTT assay. Viability assays were performed on the MDA-MB-231 cells exposed to the VNPs. Fig. 10 A shows the results for different treatments: BMV virus (black), BMV-CPT VNPs (green), CPT (red), and PBS (blue). BMV showed no significant effect on cell viability at concentrations ranging from 1 to 200 μg (5×10^3 to 6×10^4 virions per cell). However, at higher concentrations of 200 to 400 μg (8×10^4 to 2×10^6 virions per cell),

a notable increase in cell viability was observed, reaching 111% to 120% of the control value. Cancer cells, due to their high energy demand, consume large amounts of lipids, proteins, and carbohydrates, and use extracellular proteins through macroendocytosis to meet their bioenergetic needs. Viral proteins, such as the HBx protein of the HBV virus or phage MS2, can promote cell proliferation.[30–33] It is suggested that BMV capsid proteins could be used by MDA-MB-231 cells for energy production.

In the case of BMV-CPT nanocarriers, a tendency to decrease cell viability was observed between 0.5 and 20 ng μL^{-1}. However, free CPT affected cell viability with increasing concentration, but its effect was less than that of BMV-CPT nanocarriers. The trend begins at 1 ng μL^{-1} and becomes more pronounced at 12 ng μL^{-1}, where the effect of VNPs is 7% greater than the effect of the free drug ($*p < 0.005$). Fig. S10A shows the dose–response effect of BMV-CPT, the curve was adjusted and an IC_{50} of 12.82 ± 1.30 ng μL^{-1} was found.

When evaluating CCMV (Fig. 10B, black), it was observed that when incubating between 1 and 100 μg of virus, cell viability remained around 100%. However, when increasing the virus dose from 100 to 400 μg (5×10^5 to 2×10^6 virions per cell), there was a decrease of approximately 10% in cell viability. In the case of CCMV-CPT VNPs (green), a slight decrease in cell viability was evident between 0.1 and 20 ng μL^{-1}. CPT alone also compromised cell viability with increasing concentration, reaching a reduction of approximately 40% at 20 ng μL^{-1}. Fig. S10B shows the dose–response effect of CCMV-CPT. Upon curve fitting, the IC_{50} was found to be 10.39 ± 0.674 ng μL^{-1}.

In the case of CCMV, no effect on cell viability of MDA-MB-231 cells was observed when exposed to low concentrations. However, when the concentration was increased, there was a decrease of approximately 10%. Viability assays of MDA-MB-231 cells exposed to CPT-loaded VNPs showed that the drug-loaded BMV and CCMV nanocarriers had better activity than the free drug. At 10 ng μL^{-1}, the effect of VNPs is 8% greater than the effect of the free drug ($*p < 0.005$). In this study, the IC_{50} for the BMV-CPT system was determined to be 12.82 ng μL^{-1} (36.81 nM) and for the CCMV-CPT system 10.39 ng μL^{-1} (29.82 nM). Both systems were more effective than the CPT-loaded $CuCo_2S_4$ nanocarriers (IC_{50} of 68.93 ng μL^{-1}) reported by Pillai *et al.*, and more efficient than the CPT nanorods synthesized by Zhou *et al.*, who reported an IC_{50} of 665 nM.[34,35] The concentrations of BMV-CPT and CCMV-CPT used allowed the IC_{50} to be calculated, since at these values cell viability was zero.

The drug release profiles of our VNPs suggest a mechanism distinct from other platforms. Whereas FHV VLPs exhibited a classic pH-sensitive release profile—with minimal leakage (4%) at pH 7.4 and rapid release (72%) at pH 5.5 (ideal for endo/lysosomal escape) (Ghosh *et al.*, 2021)—our VNPs demonstrated significant release at physiological pH (7.4).[29] This indicates a potential for cytoplasmic release triggered by the unique disassembly kinetics of plant viral capsids in the intracellular environment, which could be particularly advantageous for drugs susceptible to lysosomal degradation.

The CCMV and BMV VNPs have superior drug retention compared to polymeric nanoparticles. Min *et al.* (2008) reported a glycolic chitosan-based CPT nanocarrier that exhibited a substantial burst release (36–45% within 9 h) at pH 7.4, reaching 86% after one week.[36] Under comparable physiological conditions, both BMV and CCMV VLPs exhibited markedly improved retention, releasing only 44.59% and 11.86% of their payload, respectively, after 24 hours. This enhanced stability is critical for minimizing premature drug leakage during systemic circulation, thereby reducing off-target toxicity.

This effective retention and delivery directly translated to enhanced cytotoxic efficacy. Unlike Min *et al.*, who found free CPT to be more cytotoxic than their encapsulated formulation in MDA-MB-231 cells,[2] we observed a significant enhancement

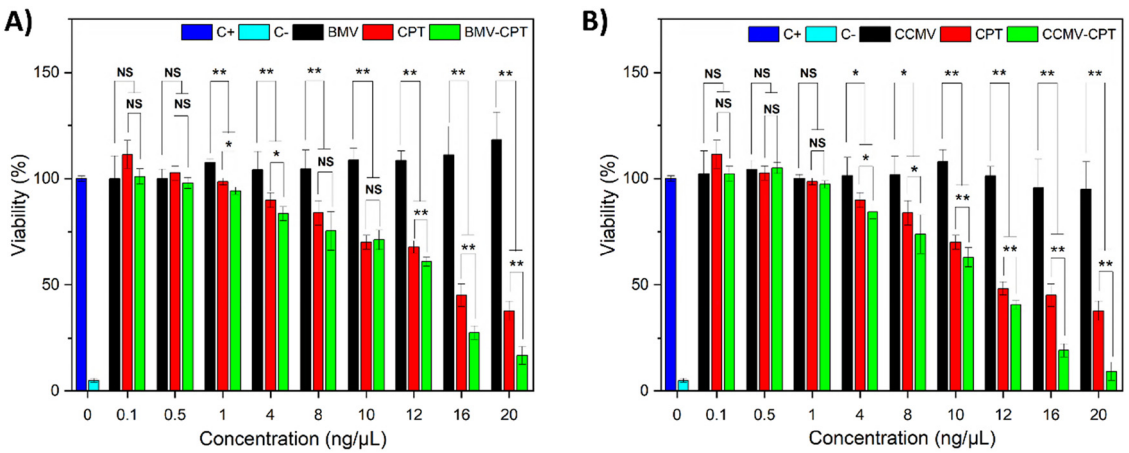

Fig. 10 Viability of MDA-MB-231 cells exposed to VNPs. (A) Viability of MDA-MB-231 cells exposed to BMV-CPT. (B) Viability of MDA-MB-231 cells exposed to CCMV-CPT. In the histograms, the results from BMV-CPT and CCMV-CPT are marked in green, and the control experiments for BMV and CCMV in black, CPT in red, PBS in blue, and DMSO is marked in cyan. The concentration shown in the graph indicates the concentration of drug loaded in the VNP. The amount of drug and virus present in the VNP determined the concentration of free drug and unloaded virus in the assay. Bars represent the average viability, and error bars represent the standard deviation (SD). Statistical analyses included One-way ANOVA and Tukey test, $*P < 0.05$, $**P < 0.005$, and NS means not significative. Means and standard deviations are reported in Table S6.

in cytotoxicity when CPT was loaded within BMV and CCMV VNPs.[36] The absence of cytotoxic effects from unloaded VLPs confirms that cell death is attributable to the efficient delivery of active CPT, suggesting the VLP architecture effectively protects the payload from extracellular inactivation and facilitates efficient intracellular delivery.

Our finding that encapsulation enhances cytotoxic potency is consistent with other nanocarrier systems. *Martins et al.*, showed that CPT-loaded solid lipid nanoparticles (SLNs, 130–160 nm) were significantly more cytotoxic against glioma cells than the free drug.[37] Similarly, Ferris *et al.*, observed a 35% increase in cell death with CPT-loaded, RGD-functionalized mesoporous silica nanoparticles compared to free CPT.[38]

The data presented herein align with this broader phenomenon and demonstrate that plant VLP nanocarriers can similarly, and in some cases more effectively, enhance the cytotoxic profile of their loaded drug.

MitoID RED assay. After the cell viability assay, we analyzed MDA-MB-231 cells exposed to VNPs at a concentration of 10 ng μL^{-1} using a fluorescence microscope (Lumascope 720, Etaluma Inc.). Fig. S11A and B show cells treated with BMV-CPT, and Fig. S11C and D show cells treated with CCMV-CPT. In both cases, damaged, dead cells (green box), and cells in a minimum energy state (blue circle) are observed. Some live cells (red arrows) attached to the damaged cells in a lower focal plane can also be identified. The MTT assay depends on mitochondrial activity to reduce formazan, so an assay was performed to observe the behavior of mitochondria in damaged cells. Fig. 11A–D show confocal micrographs of MDA-MB-231 cells treated with BMV-CPT, revealing a wide dispersion of mitochondria, especially at the periphery of the nucleus, with an intense high mitochondrial membrane potential (MMP) signal (orange), compared to the low MMP signal (green). Fig. 11E–H show the treatment with BMV, where the distribution of mitochondria is similar, with a higher intensity of high MMP. In Fig. 11I–L, mitochondria treated with CPT are less dispersed and the intensity of high MMP is like that of low MMP, indicating no damage to the mitochondrial membrane.

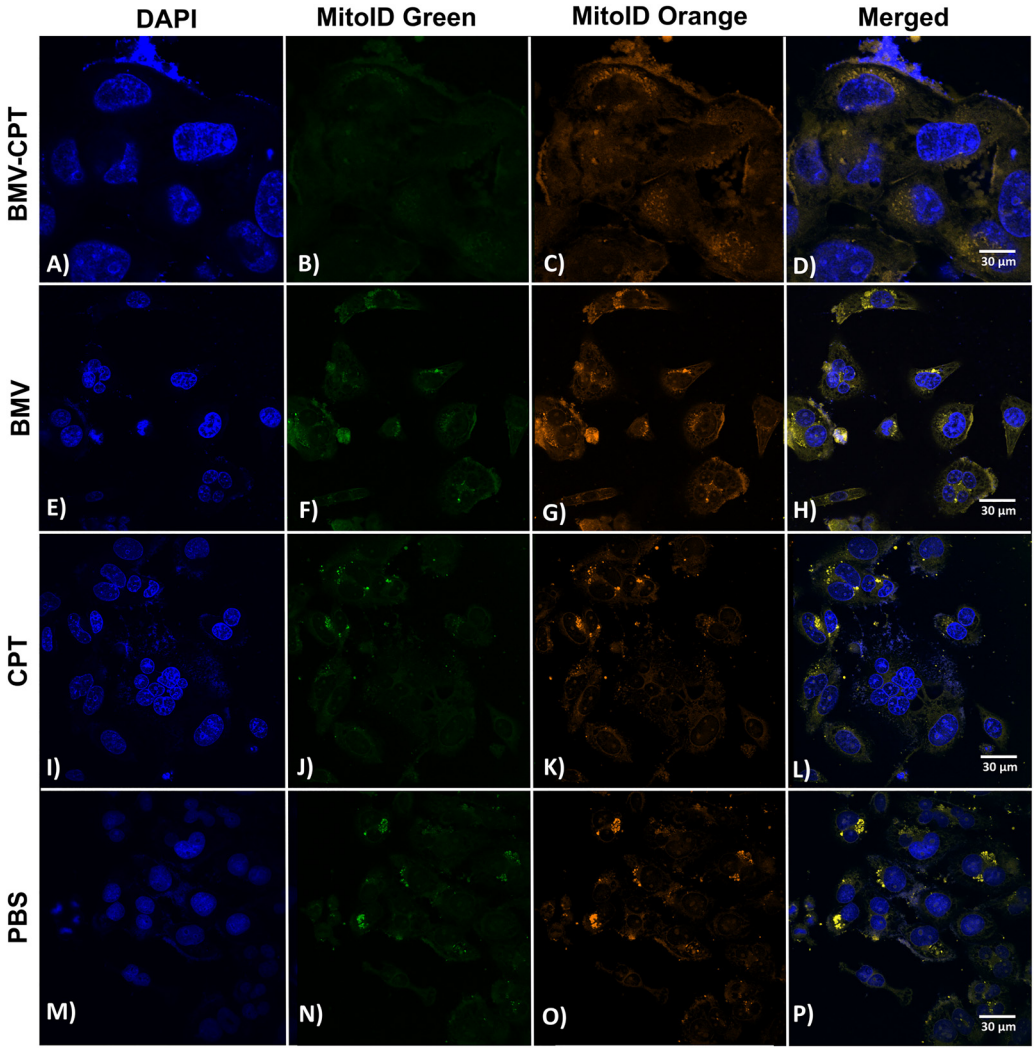

Fig. 11 MitoID assay in MDA-MB-231 cells. (A)–(D) MitoID from MDA-MB-231 cells exposed to BMV-CPT. (E)–(H) MitoID from MDA-MB-231 cells exposed to BMV. (I)–(L) MitoID from MDA-MB-231 cells exposed to CPT. (M)–(P) MitoID a from control MDA-MB-231 cells.

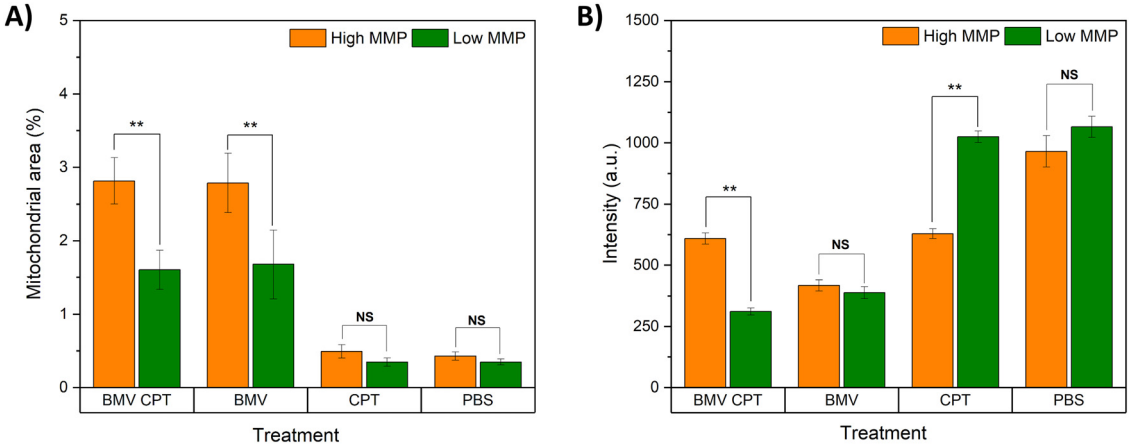

Fig. 12 MitoID results. (A) Percentage of mitochondrial area within MDA-MB-231 cells. (B) Average mitochondrial fluorescence intensities within MDA-MB-231 cells. Bars represent the average, and error bars represent the standard deviation (SD). Statistical analyses included One-way ANOVA and Tukey test, $^{**}P < 0.005$, and NS means not significative. Means and standard deviations are reported in Table S7.

Fig. 11M–P, corresponding to the control, show a low dispersion of mitochondria, with similar high and low MMP signals.

Image analysis with ImageJ® showed that all treatments had a larger orange fluorescent area, indicating that the cells have a permeable membrane; however, the ANOVA separates BMV and BMV-CPT treated cells as they had a greater mitochondrial area with high MMP (orange), indicating that the mitochondrial membrane is more permeable. Cells treated with BMV and BMV-CPT showed a mitochondrial area 5.7 times greater than those treated with CPT and PBS (Fig. 12A). With respect to fluorescence intensity, cells treated with BMV-CPT showed a significantly higher signal in the orange channel (high MMP) compared to the green signals (low MMP) (Fig. 12B). According to Parrott *et al.*, as mitochondria become more activated, the MitoID signal in the orange channel increases, which is associated with increased mitochondrial membrane permeability. The results suggest that BMV-CPT increases mitochondrial permeability.[39]

Mitochondrial membrane potential is a key indicator of cellular viability, as it is essential for ATP production *via* oxidative phosphorylation. Mitochondrial dysfunction can trigger a cascade of events, including the release of pro-apoptotic factors, such as cytochrome *c*, into the cytosol, which activates cascades and initiates apoptosis. In addition, prolonged mitochondrial damage can result in a decrease in ATP production and the generation of reactive oxygen species (ROS). The orange fluorescence of JC-1 indicates high membrane potential. When BMV-CPT treated cells are compared to control cells, changes in mitochondrial activity are observed, suggesting that exposure to the treatment causes mitochondrial damage, which can lead to cell death.[40,41]

The use of viral nanoparticles as drug delivery vehicles has gained significant interest due to their innate cell-entry capabilities and low cytotoxicity associated with capsid proteins. Numerous icosahedral viruses and virus-like particles (VLPs)—including CPMV, CCMV, PhMV, rotavirus VP6, and bacteriophage P22—have been loaded or conjugated with doxorubicin (DOX) and evaluated for antitumor efficacy. These platforms consistently demonstrated cytotoxicity greater than or comparable to that of free DOX, underscoring their potential as targeted delivery systems in cell lines such as HeLa, HepG2, and MCF-7.[42–46] Beyond icosahedral viruses, filamentous variants have also been explored. For example, tobacco mosaic virus (TMV) was internally loaded with cisplatin and shown to exert superior cytotoxicity against ovarian cancer cells compared to free cisplatin.[47] Similarly, potato virus X (PVX) was externally conjugated with a tumor necrosis factor-related apoptosis-inducing ligand (TRAIL), effectively inducing caspase-mediated apoptosis and reducing tumor growth in models of triple-negative breast cancer.[48]

While these studies highlight the broad utility of viral platforms in targeted therapy, they primarily exploit self-assembly properties and often rely on chemical conjugation of therapeutics. In contrast, the approach presented in this work leverages the inherent electrostatic landscape of the capsid interior to load hydrophobic drugs *via* self-assembly, eliminating the need for covalent modification of the capsid protein.

Conclusion

BMV and CCMV VLPs were successfully infused with the hydrophobic cancer drug CPT in water miscible solvents after which they were transferred to aqueous buffer solutions while preserving their association with hundreds of drug molecules per capsid. DMSO was the most suitable solvent for loading drugs into VLPs with minimal alteration of virion size or morphology. Other solvents, such as ethanol and methanol, destabilized the viral capsid, especially at high solvent molar fractions. Cancer cell entry assays highlighted the potential of viral capsids as drug carriers for the treatment of breast cancer, the leading cause of cancer death in women.

The strong agreement between the *in silico* predictions and the experimental results for CPT loading demonstrates that computational docking can effectively could reduce the time

and costs of preliminary screening for compatible drug-VLP systems. It was found that in the protein–drug complex there are affinity energies close to those found in biological environments, with predominantly hydrophobic interactions and some hydrogen bonds. CPT can be transported in aqueous media through hydrophobic interactions in BMV and CCMV viral particles. In the synthesis of VNPs, both the amount of drug loaded and the release profile according to pH were evaluated. BMV showed a 29.5% higher loading capacity of CPT compared to CCMV, which is consistent with the *in silico* results. TEM images revealed that BMV expanded up to 19% upon CPT loading. Cellular assays demonstrated the internalization of VNPs, and decreased cell viability. Both BMV and CCMV, as well as their CPT-loaded VNPs, were able to internalize into the cytosol and nucleus of MDA-MB-231 cancer cells. This is a very important finding in the controlled delivery of drugs, as many require internalization into the nucleus to exert their effect. Such is the case with the evaluated chemotherapeutic molecule, camptothecin, which blocks the TOP1 enzyme at the replication fork. VNPs showed better *results in vitro* than the free drug in breast cancer cell line. BMV-CPT increased the mitochondrial membrane potential (MMP) in MDA-MB-231 cells, and a high mitochondrial membrane potential implies that mitochondrial respiration becomes a significant producer of reactive oxygen species (ROS) which are potentially harmful to cells. These results underline the capacity of viral capsids as effective carriers for anticancer nuclei drugs in the treatment of breast cancer.

Author contributions

Formal analysis: E. L. G., C. M. V., and R. D. C. N.; funding acquisition: R. D. C. N.; investigation: E. L. G., M. M. H. H., C. M. V., M. L. T., B. D., J. R. G., A. G. R. H., and R. D. C. N.; methodology: E. L. G., P. G. J. F., B. D., and R. D. C. N.; project administration: R. D. C. N.; resources: R. D. C. N.; supervision: R. D. C. N.; writing – original draft: ELG. and R. D. C. N.; writing – review and editing: E. L. G., P. G. J. F., B. D., J. R. G., A. G. R. H., M. L. T., and R. D. C. N.

Conflicts of interest

The authors reported no conflicts of interest.

Data availability

Software and computational resources: Statistical analysis. Shapiro-Wilk Test: **https://www.statskingdom.com/shapiro-wilk-test-calculator.html**. One-way ANOVA and Tukey's test: **http://vassarstats.net/anova1u.html**. Computational experiment: Autodock Vina® 1.2: https://vina.scripps.edu/. PyMOL® 3.1.2: **https://pymol.org/**. LigPlot+® 2.2: **https://www.ebi.ac.uk/thornton-srv/software/LigPlus/**. CPT molecule PubChem® ID: 24360: **https://pubchem.ncbi.nlm.nih.gov/compound/camptothecin**. BMV protein PDB® 3J7L: **https://www.rcsb.org/structure/3J7L**. CCMV protein PDB® 1ZA7: **https://www.rcsb.org/structure/1ZA7**.[49,50]

Supporting information: Autodock vina Results: **https://drive.google.com/drive/folders/14dhGWdpvFTHfv8mawMmKbOJQu6un2BLg?usp=drive_link**. PyMOL and LigPlot Results: **https://drive.google.com/drive/folders/1ET4IcOZU0TII209BqwrChr7Sg0tW2jwV?usp=drive_link**. Data of experiments: All results are found in an opju file and sorted by folder between each of the experiments. **https://drive.google.com/drive/folders/1oMKxu2aAY9sbaNgiXQKZjvQyqDuG2nNP?usp=drive_link**.

Supplementary information (SI) is available. See DOI: **https://doi.org/10.1039/d5ma00261c**.

Acknowledgements

This work was supported by the UNAM DGAPA PAPIIT-IT101822. We thank Dr Oscar González-Davis, MSc Itandehui Betanzo for their technical assistance, and Dr Diego Delgado and Dr Gabriela Guzmán for their help with the confocal microscope and TEM, respectively. B. D. acknowledges support from a PNRR/2022/C9/MCID/18 award.

References

1 S. H. Hassanpour and M. Dehghani, *J. Cancer Res. Pract.*, 2017, **4**, 127–129.
2 A. Dri, G. Arpino, G. Bianchini, G. Curigliano, R. Danesi, M. De Laurentiis and F. Puglisi, *Cancer Treat. Rev.*, 2024, **123**, 102672.
3 A. G. Waks and E. P. Winer, *JAMA*, 2019, **321**, 288–300.
4 T. Furuta, H. Takemura, Z. Y. Liao, G. J. Aune, C. Redon, O. A. Sedelnikova and Y. Pommier, *J. Biol. Chem.*, 2003, **278**, 20303–20312.
5 C. J. Thomas, N. J. Rahier and S. M. Hecht, *Bioorg. Med. Chem.*, 2004, **12**, 1585–1604.
6 M. Ghanbari-Movahed, T. Kaceli, A. Mondal, M. H. Farzaei and A. Bishayee, *Biomedicines*, 2021, **9**, 480.
7 M. Loredo-Tovias, A. L. Duran-Meza, M. V. Villagrana-Escareño, R. Vega-Acosta, E. Reynaga-Hernández, Ll. M. Flores-Tandy, O. E. Valdes-Resendiz, R. D. Cadena-Nava, E. R. Alvizo-Paez and J. Ruiz-Garcia, *Nanoscale*, 2017, **9**, 11625–11631.
8 Z. Cheng, Y. Huang, Q. Shen, Y. Zhao, L. Wang, J. Yu and W. Lu, *Eur. J. Med. Chem.*, 2021, **226**, 113851.
9 Y. H. Chung, H. Cai and N. F. Steinmetz, *Adv. Drug Delivery Rev.*, 2020, **156**, 214–235.
10 J. Bujarski, D. Gallitelli, F. García-Arenal, V. Pallás, P. Palukaitis, M. K. Reddy and A. Wang, *J. Gen. Virol.*, 2019, **100**(8), 1206–1207.
11 A. Nuñez-Rivera, P. G. Fournier, D. L. Arellano, A. G. Rodriguez-Hernandez, R. Vazquez-Duhalt and R. D. Cadena-Nava, *Beilstein J. Nanotechnol.*, 2020, **11**, 372–382.
12 A. M. Wen and N. F. Steinmetz, *Chem. Soc. Rev.*, 2016, **45**, 4074–4126.
13 B. X. Hoang, H. Q. Hoang and B. Han, *Med. Hypotheses*, 2020, **143**, 109866.

14 W. R. Moorer, *Int. J. Dent. Hyg.*, 2003, 138–142.
15 J. C. Chan and H. H. Gadebusch, *Appl. Microbiol.*, 1968, **16**, 1625–1626.
16 P. C. Agu, C. A. Afiukwa, O. U. Orji, E. M. Ezeh, I. H. Ofoke, C. O. Ogbu and P. M. Aja, *Sci. Rep.*, 2023, **13**, 13398.
17 T. H. Hasan, H. A. Kadhum and K. K. Alasedi, *Int. J. Pharm. Res.*, 2021, **13**, 2151–2152.
18 C. Meyers, R. Kass, D. Goldenberg, J. Milici, S. Alam and R. Robison, *J. Hosp. Infect.*, 2021, **107**, 45–49.
19 A. Xie, I. Tsvetkova, Y. Liu, X. Ye, P. Hewavitharanage, B. Dragnea and R. D. Cadena-Nava, *Bioconjugate Chem.*, 2021, **32**, 2366–2376.
20 K. M. Bond, N. A. Lyktey, I. B. Tsvetkova, B. Dragnea and M. F. Jarrold, *J. Phys. Chem. B*, 2020, **124**, 2124–2131.
21 A. P. Wanguyun, W. Oishi and D. Sano, *Food Environ. Virol.*, 2024, 1–13.
22 J. Lu, C. Liu, P. Wang, M. Ghazwani, J. Xu, Y. Huang and S. Li, *Biomaterials*, 2015, **62**, 176–187.
23 H. Zhan, H. Zhao, N. Muhammad, T. Li, Y. Liu and J. Wang, *Nanotechnology*, 2019, **31**, 075101.
24 J. M. Fox, G. Wang, J. A. Speir, N. H. Olson, J. E. Johnson, T. S. Baker and M. J. Young, *Virology*, 1998, **244**, 212–218.
25 K. W. Adolph, *J. Gen. Virol.*, 1975, **28**, 147–154.
26 J. A. Speir, S. Munshi, G. Wang, T. S. Baker and J. E. Johnson, *Structure*, 1995, **3**, 63–78.
27 K. Chauhan, C. N. Olivares-Medina, M. V. Villagrana-Escareño, K. Juárez-Moreno, R. D. Cadena-Nava, A. G. Rodríguez-Hernández and R. Vazquez-Duhalt, *ChemMedChem*, 2022, **17**(19), e202200384.
28 P. Gama, R. D. Cadena-Nava, K. Juárez-Moreno, J. Pérez-Robles and R. Vazquez-Duhalt, *ChemMedChem*, 2021, **16**(9), 1438–1445.
29 S. Ghosh and M. Banerjee, *Sci. Rep.*, 2021, **11**, 7030.
30 W. Wu, S. C. Hsiao, Z. M. Carrico and M. B. Francis, *Angew. Chem.*, 2009, **48**, 9493.
31 H. Su, F. Yang, B. Sun and M. Karin, *Autophagy*, 2021, **17**, 1290–1291.
32 L. M. Butler, Y. Perone, J. Dehairs, L. E. Lupien, V. de Laat, A. Talebi and J. V. Swinnen, *Adv. Drug Delivery Rev.*, 2020, **159**, 245–293.
33 Y. Du, G. Kong, X. You, S. Zhang, T. Zhang, Y. Gao and X. Zhang, *J. Biol. Chem.*, 2012, **287**, 26302–26311.
34 A. S. Pillai, A. Alexander, V. Manikantan, G. S. Varalakshmi, B. A. Akash and I. V. Enoch, *J. Cluster Sci.*, 2023, **34**, 2991–2999.
35 Z. Zhou, Y. Piao, L. Hao, G. Wang, Z. Zhou and Y. Shen, *Nanoscale*, 2019, **11**, 15907–15916.
36 K. H. Min, K. Park, Y. S. Kim, S. M. Bae, S. Lee, H. G. Jo and I. C. Kwon, *J. Controlled Release*, 2008, **127**, 208–218.
37 S. M. Martins, B. Sarmento, C. Nunes, M. Lúcio, S. Reis and D. C. Ferreira, *Eur. J. Pharm. Biopharm.*, 2013, **85**, 488–502.
38 D. P. Ferris, J. Lu, C. Gothard, R. Yanes, C. R. Thomas, J. C. Olsen and J. I. Zink, *Small*, 2011, **7**, 1816–1826.
39 J. M. Parrott, T. Oster and H. Y. Lee, *iScience*, 2021, **24**(11), 103293.
40 L. D. Zorova, V. A. Popkov, E. Y. Plotnikov, D. N. Silachev, I. B. Pevzner, S. S. Jankauskas and D. B. Zorov, *Anal. Biochem.*, 2018, **552**, 50–59.
41 K. Jiang, W. Wang, X. Jin, Z. Wang, Z. Ji and G. Meng, *Oncol. Rep.*, 2015, **33**, 2711–2718.
42 A. A. Aljabali, S. Shukla, G. P. Lomonossoff, N. F. Steinmetz and D. J. Evans, *Mol. Pharmaceutics*, 2013, **10**, 3–10.
43 I. Barwal, R. Kumar, S. Kateriya, A. K. Dinda and S. C. Yadav, *Sci. Rep.*, 2016, **6**, 37096.
44 H. Hu and N. F. Steinmetz, *Biotechnol. J.*, 2020, **15** 2000077.
45 Q. Zhao, W. Chen, Y. Chen, L. Zhang, J. Zhang and Z. Zhang, *Bioconjugate Chem.*, 2011, **22**, 346–352.
46 H. Kim, H. Choi, Y. Bae and S. Kang, *Biotechnol. Bioeng.*, 2019, **116**, 2843–2851.
47 C. E. Franke, A. E. Czapar, R. B. Patel and N. F. Steinmetz, *Mol. Pharmaceutics*, 2017, **15**, 2922–2931.
48 D. H. Le, U. Commandeur and N. F. Steinmetz, *ACS Nano*, 2019, **13**, 2501–2510.
49 J. A. Speir, B. Bothner, C. Qu, D. A. Willits, M. J. Young and J. E. Johnson, *J. Virol.*, 2006, **80**, 3582–3591.
50 Z. Wang, C. F. Hryc, B. Bammes, P. V. Afonine, J. Jakana, D. H. Chen, X. Liu, M. L. Baker, C. Kao, S. J. Ludtke, M. F. Schmid, P. D. Adams and W. Chiu, *Nat. Commun.*, 2014, **5**, 4808.